Biochemistry **1999,** *38,* 12681−12689

Identification of Dimethylbenzimidazole Axial Coordination and Characterization of ^{14}N Superhyperfine and Nuclear Quadrupole Coupling in Cob(II)alamin Bound to Ethanolamine Deaminase in a Catalytically-Engaged Substrate Radical−Cobalt(II) Biradical State†

Shyue-Chu Ke,‡ Maricel Torrent,§ Djamaladdin G. Museav,§ Keiji Morokuma,§ and Kurt Warncke*,‡

Department of Physics, 1001 Rollins Research Center, 1510 Clifton Road, Emory University, Atlanta, Georgia 30322, and Cherry L. Emerson Center for Scientific Computation and Department of Chemistry, Emory University, Atlanta, Georgia 30322

Received December 30, 1998; Revised Manuscript Received July 12, 1999

ABSTRACT: Cobalt(II)−^{14}N superhyperfine and ^{14}N nuclear quadrupole couplings in cryotrapped free and ethanolamine deaminase-bound cob(II)alamin have been characterized in the disordered solid state by using X-band electron spin−echo envelope modulation (ESEEM) spectroscopy. Enzyme-bound cob(II)alamin was cryotrapped after formation by substrate-initiated, thermally activated cleavage of the cobalt−carbon bond of adenosylcobalamin. Free dimethylbenzimidazole axial base-on cob(II)alamin was formed by photolysis of the corresponding adenosylcobalamin and cryotrapped in glycerol−aqueous glass. Three-pulse ESEEM experiments were performed by using microwave pulse excitation at the $g_\perp$ value of Co^{II} at magnetic field values of 287.0 and 345.0 mT and over a range of τ values from 227 to 1316 ns. Two common sets of ^{14}N features are distinguished in the ESEEM spectra. One set is assigned to the remote (N1) nitrogen in the dimethylbenzimidazole α-axial ligand by using two independent approaches: (a) comparison of ESEEM from cob(II)alamin with ESEEM from cob(II)inamide−ligand model compounds and (b) from the correspondence between the N1 ^{14}N nuclear quadrupole parameters derived from ESEEM simulations and those computed by using density functional theory. The second set is assigned to the corrin ring ^{14}N nuclei. The results identify the coenzyme's on-board dimethylbenzimidazole moiety as the α-axial ligand to cob(II)alamin in ethanolamine deaminase in the substrate radical−Co^{II} biradical catalytic intermediate state. Thus, Co^{II} is a pentacoordinate, α-axial liganded complex during turnover. We infer that dimethylbenzimidazole is also the α-axial ligand to the intact coenzyme in the resting enzyme. A 14% increase in the isotropic hyperfine coupling of the remote dimethylbenzimidazole ^{14}N nucleus in enzyme-bound versus free base-on cob(II)alamin shows an enhanced delocalization of unpaired spin density from Co^{II} onto the axial ligand, which would contribute to the acceleration of the cobalt−carbon bond cleavage rate in situ.

Vitamin B$_{12}$ coenzyme [adenosylcob(III)alamin or adenosylcobalamin] functions as the initiator of radical-mediated substrate rearrangement reactions in the family of vitamin B$_{12}$ coenzyme-dependent enzymes (*1*−*5*). These enzymes are distinguished by the catalysis of carbon skeleton rearrangements (class I enzymes; glutamate, methyleneglutarate, and methylmalonyl-CoA mutases), heteroatom elimination reactions (class II; diol dehydrase, glycerol dehydrase, ethanolamine deaminase, ribonucleotide triphosphate reductase), and pyridoxal phosphate-assisted amine group rearrangements (class III; lysine and ornithine aminomutases) (*4*). In the common first step of the catalytic cycle, homolytic cleavage of the cobalt−carbon bond leads to formation of the 5′-deoxyadenosyl radical and paramagnetic low-spin ($S = {}^{1}/_{2}$) Co^{II} in cob(II)alamin. The bound substrate is activated for rearrangement by direct abstraction of a hydrogen atom by the 5′-deoxyadenosyl radical (*1*−*3*, *6*), or via a 5′-deoxyadenosyl-generated cysteine thiyl (*5*, *7*, *8*) or other protein radical (*9*) in the different systems. Following rearrangement, the reverse of the hydrogen transfer step(s) occurs to form the diamagnetic product, and the re-formed 5′-deoxyadenosyl radical recombines with Co^{II} to regenerate the intact coenzyme.

One of the remarkable features of protein guidance of reactivity in the vitamin B$_{12}$ coenzyme-dependent enzymes is the acceleration of the effective cobalt−carbon bond cleavage rate by approximately 10^{12}-fold relative to the rate for the free coenzyme in solution (*10*, *11*). This large enhancement of radical pair yield has been proposed to receive contributions from substrate-derived radical formation (*12*−*15*). Proposals have also been advanced for contributions to the cleavage rate acceleration from specific interactions of the cobalamin moiety with the protein, as recently

---

† This work was supported by Grant DK-54514 from the National Institutes of Health (K.W.) and Grant CHE96-27775 from the National Science Foundation (K.M.)

* Corresponding author. Tel: 404-727-2975. Fax: 404-727-0873. E-mail: kwarncke@physics.emory.edu.

‡ Department of Physics.

§ Cherry L. Emerson Center for Scientific Computation and Department of Chemistry.

10.1021/bi983067w CCC: $18.00

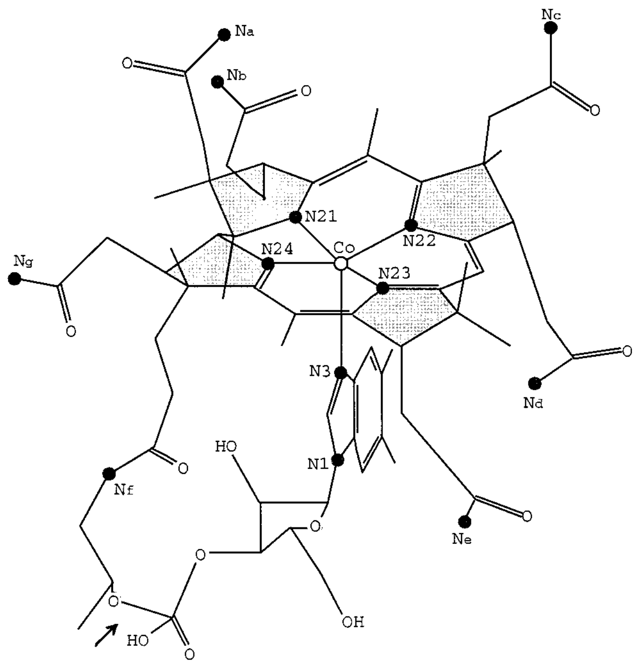

FIGURE 1: Depiction of cob(II)alamin from the structure of adenosylcobalamin determined by X-ray crystallography (*18*). Cob(II)alamin is shown in the dimethylbenzimidazole axial "base-on" form. The α- and *β*-faces of the corrin ring are depicted as the lower and upper sides of the macrocycle. In cob(II)inamides, the nucleotide loop is severed at the position marked by the arrow. The positions of nitrogen nuclei are highlighted with filled circles. The amide nitrogens are denoted with letter subscripts, and the five-membered rings containing each corrin ring nitrogen nucleus are shaded for clarity. The five-member rings associated with each corrin ring nitrogen are denoted A (N21), B (N22), C (N23), and D (N24). "Butterfly-bending" of the corrin ring occurs about the bisector of the N24,N23 and N21,N22 halves of the ring system (*18*).

summarized (*16*, *17*). Our broad aim is to reveal protein-specific effects on cob(II)alamin structure and reactivity by using techniques of high spectral resolution electron paramagnetic resonance (EPR)[1] spectroscopy to characterize the structure of the coenzyme in enzyme engaged in catalytic turnover. This entails investigation of the cob(II)alamin moiety in biradical states of the enzyme.

The structure of free cob(II)alamin in the axial "base-on" state is shown in Figure 1 (*18*, *19*). The central Co^{II} is coordinated equatorially by the four nitrogen atoms at the inner edge of the corrin ring. The dimethylbenzimidazole α-axial ligand includes a secondary, imino nitrogen (proximal nitrogen, N3) that directly coordinates Co^{II} and a tertiary, amino nitrogen (remote nitrogen, N1) that is bonded to the nucleotide loop that links the axial base to the corrin ring. Protein-induced modifications of the length of the dimethylbenzimidazole $N3-Co^{II}$ bond have been proposed (*20*−*24*) to sterically modulate the pucker, or "butterfly bending" (*18*), of the quasi-flexible corrin ring. In this mechanism, compression of the $Co^{II}-N3$ bond leads to increased steric hindrance between the bulky dimethylbenzimidazole and the α-face of the corrin ring, which increases upward bending of the macrocycle. This causes steric strain in the deoxyadenosyl 5′-carbon−cobalt bond on the *β*-face of the corrin, which weakens the bond. In support of the mechanochemical principle (*20*) underlying this model, dimethylbenzimidazole enhances the upward folding of the corrin ring relative to the smaller imidazole as axial ligand (*25*), even in the absence of protein. However, in findings that appear to dimish the importance of this type of steric trans-effect in the carbon skeleton-rearranging enzymes, X-ray crystallographic and EPR spectroscopic studies have shown that axial coordination by dimethylbenzimidazole in the free coenzyme is supplanted by the smaller imidazole group of a protein histidine residue in the methylcobalamin-dependent methionine synthase (*26*, *27*) and in the adenosylcobalamin-dependent enzymes, methylmalonyl CoA mutase (*28*, *29*) and glutamate mutase (*30*). The carbon skeleton-rearranging enzymes contain a consensus amino acid sequence that includes the liganding histidine residue (*26*, *31*, *32*) that is absent in the enzymes that conduct heteroatom elimination reactions (*33*−*37*). Indeed, EPR studies have shown that dimethylbenzimidazole is retained as the α-axial ligand in diol dehydrase (*37*) and ribonucleotide triphosphate reductase (*38*). The identity of the α-axial ligand in ethanolamine deaminase, an otherwise biochemically well-characterized vitamin B_{12} coenzyme-dependent enzyme (*1*−*3*, *39*), has not been reported.

The identity of the α-axial ligand to cob(II)alamin bound in *Salmonella typhimurium* ethanolamine deaminase (*33*, *40*) and protein-induced changes in cob(II)alamin structure are addressed in these studies by comparing $Co^{II}-{}^{14}N$ superhyperfine and ^{14}N nuclear quadrupole coupling in enzyme-bound and free-solution cob(II)alamin cryotrapped in the disordered solid state. The enzyme-bound cob(II)alamin is formed by substrate-initiated, thermally activated cobalt−carbon bond cleavage (*39*). The observed substrate radical−Co^{II} biradical state is a proven kinetically competent intermediate in catalysis (*41*). Although the $Co^{II}-N3$ coupling is resolved in continuous-wave (CW) EPR spectra of free base-on cob(II)alamin in the solid state (*42*), weaker $Co^{II}-{}^{14}N$ interactions, such as those with the corrin ring and N1 nitrogen nuclei, are obscured by inhomogeneous line-broadening. Further, in the ethanolamine deaminase-bound cob(II)alamin, no Co^{II} hyperfine or ^{14}N superhyperfine couplings are resolved in solid-state EPR spectra, owing to additional line-broadening from the Co^{II}−substrate biradical interaction (*41*, *43*). We have therefore used the high-spectral resolution electron spin−echo envelope modulation (ESEEM) technique of pulsed-EPR spectroscopy (*44*, *45*) to measure $Co^{II}-{}^{14}N$ superhyperfine couplings in cob(II)alamin. Our strategy for identifying the α-axial ligand begins with the detection of ESEEM spectral features arising from hyperfine coupling between Co^{II} and the remote nitrogen (N1) of the axial ligand in free and enzyme-bound cob(II)alamin. The N1 nitrogen is targeted because the alkylated dimethylbenzimidazole and unsubstituted imidazole N1 centers are expected to provide distinctive ^{14}N nuclear quadrupole interaction signatures in the ESEEM spectra (*46*−*48*). The spectral assignment is performed by using two independent methods. In one method, the ESEEM spectra of cob(II)alamin are compared with spectra obained for model cob(II)inamide−ligand complexes, where truncation of the nucleotide tail, at the position shown by the arrow in Figure 1, allows axial ligation by externally added imidazole and 1-methylbenzimidazole. In a second method, identification of the origin of the axial base is accomplished by

---

[1] Abbreviations: EPR, electron paramagnetic resonance; ESEEM, electron spin−echo envelope modulation.

comparison of the ^{14}N nuclear quadrupole parameters, obtained from ESEEM simulations, with parameters for the model ligands that are computed by using density functional theory (*49*).

The results demonstrate directly, for the first time, that dimethylbenzimidazole is the axial ligand to cob(II)alamin in ethanolamine deaminase. The enzyme-bound cob(II)alamin is formed by the native route of cobalt−carbon bond homolysis and is present in a true catalytic intermediate state (*39*, *41*), in contrast to the photolytic or inhibitor-associated cob(II)alamin formation in inactivated enzyme in the other vitamin B_{12} coenzyme-dependent enzymes where the identity of the axial ligand has been investigated (*28*−*30*, *37*, *38*). Evidence presented for the influence of the protein on cob(II)alamin structure therefore corresponds directly to the functioning system.

EXPERIMENTAL PROCEDURES

Preparations. Vitamin B_{12} coenzyme (adenosylcob(III)alamin; Sigma Chemical Co.) was dissolved at a concentration of 1 mM in 1:1 v/v glycerol−water solutions containing 10 mM potassium phosphate as buffer, loaded into 4 mm o.d. EPR sample tubes, and deaerated by successive vacuum/argon gas cycles. The pH value of the solution was adjusted to 7.0 to maintain the axially coordinated dimethylbenzimidazole (base-on form). The effective p*K* for the base-on to base-off equilibrium is 3.3−3.5 (*50*, *51*). The coenzyme in anearobic solution was then irradiated for approximately 5 min at a distance of 2−3 dm with a 150 W incandescent lamp or with the water- and glass-filtered output of a 1 kW Xe−Hg arc lamp (Oriel). The solution was frozen to a glass by immersion of the EPR tube in liquid−nitrogen-chilled isopentane solution. The cobinamide−ligand complexes were prepared similarly, with the exception that 1−2 mM methylcobinamide−perchlorate (gift of Professor Luigi Marzilli, Department of Chemistry, Emory University) was photolyzed in the presence of 1 M ligand.

Ethanolamine deaminase was purified from the *Escherichia coli* overexpression strain incorporating the cloned *Salmonella typhimurium* ethanolamine deaminase coding sequences (*33*) essentially as described (*40*), with the exception that the enzyme was dialyzed against buffer containing 100 mM HEPES (pH 7.45), 10 mM KCl, 5 mM dithiothreitol, 10 mM urea, and 10% glycerol (*52*). Enzyme activity was assayed as described (*52*) by using the sensitive 3-methylbenzothiazolinone hydrazone colorimetric method for measurement of acetaldehyde production (54). The activity of the purified enzyme with aminoethanol was 20−30 mmol/(min/mg).

Ethanolamine deaminase-bound cob(II)alamin was generated by freezing mixtures of enzyme (60 μM enzyme, 120 mM active sites), adenosylcobalamin (120 mM, 1:1 with active sites), and the substrate analogue, 2-aminopropanol (30−50 mM), mixed in buffer containing 100 mM HEPES (pH 7.45), 10 mM KCl, and 5 mM dithiothreitol (15). The Co^{II}−substrate radical pair state was trapped in high yield by immersing 4 mm o.d. EPR tubes containing the reaction mixture in the steady state in liquid-nitrogen-chilled isopentane within 15 s of mixing. Spin counts performed with diphenylpicrylhydrazyl (DPPH) as standard show that 0.6 substrate-derived radicals are present per active site. The cob(II)alamin/active site ratio is assumed to be comparable.

EPR Spectroscopy. EPR spectra were obtained by using a Bruker ER200D EPR spectrometer equipped with a Bruker 4102ST/8216 TE102 cavity, HP 4256L frequency counter, Varian V3603 electromagnet and Fieldial Mark I regulator/power supply, and Air Products cryostat and temperature controller modified for nitrogen gas flow sample cooling.

ESEEM Spectroscopy. ESEEM was collected by using a home-built wide band pulsed-EPR spectrometer that will be described elsewhere (Warncke, K., manuscript in preparation). The reflection microwave probe (*55*) featured folded half-wave microwave resonators (*56*). The ESEEM was collected by using the three-pulse ($\pi/2-\tau-\pi/2-T-\pi/2$) microwave pulse sequence (*43*, *44*) with the microwave pulse-swapping and phase-cycling sequence (*57*, *58*). τ values were selected in the three-pulse ESEEM experiments to suppress envelope modulation from matrix protons or to achieve suppression effects among the ^{14}N superhyperfine modulation contributions that proved useful in assigning conjugate features arising from the $m_s = +^1/_2$ and $m_s = -^1/_2$ manifolds of the same nucleus (*47*, *59*). The τ values sampled covered the range from 227 to 1316 ns. Envelope modulation collected from 0.2 to 5.2 ms was deadtime-reconstructed (*60*) and Fourier transformed. Envelope modulation collected using long τ values (>250 ns) was also processed prior to Fourier transformation by removing the 40−60 ns amplitude trough in the pulse-crossover segment centered at τ, and by correcting for the phase memory time-dominated echo decay in the modulation segment before pulse crossover. All data processing and analysis were performed with routines written by using Matlab (Mathworks, Nantick, MA) and run on Silicon Graphics Indigo2 or PowerMacintosh computers.

ESEEM Simulations. The coupled electron−nuclear spin system was described by the following stationary-state Hamiltonian:

$$H = \beta_e \mathbf{S}\cdot\mathbf{g}_e\cdot\mathbf{B}_0 + h\mathbf{S}\cdot\mathbf{A}\cdot\mathbf{I} - g_n\beta_n\mathbf{B}_0\cdot\mathbf{I} + \mathbf{I}'\cdot\mathbf{Q}\cdot\mathbf{I}' \quad (1)$$

where g_e, β_e and g_n, β_n are the electron and nuclear *g*-value and magneton, respectively, $\mathbf{g}_e$ is the electron **g**-tensor, $\mathbf{B}_0$ is the external magetic field vector, *h* is Planck's constant, **A** is the hyperfine interaction tensor, **Q** is the quadrupole interaction tensor, and the **S** and **I** are electron and nuclear spin operators. In the strong field approximation, the electron Zeeman interaction is given by $g_e\beta_e S_z'$, where S_z' is the fictitious spin operator (*61*, *62*). In the case of the axially symmetric Co^{II} complexes considered here, it is assumed that a range of orientations of the complex with respect to the external field are represented at the $g_\perp$ position (*63*), at which the ESEEM experiments were performed, as done previously in ESEEM simulations (*46*).

The eigenvalues and eigenvectors of the electron−nuclear part of the Hamiltonian (last three terms on the right-hand side of eq 1) were obtained by separate diagonalization of the submatrix representations corresponding to the $m_s = +^1/_2$ and $m_s = -^1/_2$ electron spin manifolds. The random orientation of electron−nuclear vectors relative to the external magnetic field direction is represented by a spherical average, which is performed independently for each coupled nucleus. The pulse time-domain ESEEM was simulated by direct application of the density matrix formalism of Mims (*59*, *64*). In this formalism, the eigenvalues and eigenvectors of the electron−nuclear part of the Hamiltonian are used to

Table 1: $\mathrm{Co^{II}}$−^{14}N Superhyperfine and ^{14}N Nuclear Quadrupole Coupling Parameters for the N1 Nitrogen Nucleus in Free and Ethanolamine Deaminase-Bound Cob(II)alamin Determined from ESEEM Simulations[a]

state	A_{iso} (MHz)	r_{eff} (Å)[b]	e^2qQ (MHz)[c]	η[d]	[α, β, γ] (deg)[e]
enzyme-bound	2.15 ± 0.05	3.0	3.20	0.12	[0, 60, 0]
free, base-on	1.85 ± 0.05	3.0	3.12	0.07	[0, 70, 0]

[a] See Experimental Section for explanation of the limits for all simulation parameter values. [b] Effective electron−nuclear separation distance in the point−dipole approximation. The distance is rendered "effective" by dipolar contributions from unpaired spin density delocalized to the axial ligand. The limits on r_{eff} values are ±0.05 Å. [c] Limits are ±0.1 MHz. [d] Limits are ±0.05. [e] Limits are ±5°.

determine the envelope modulation frequencies and intensities, respectively. For enzyme-bound cob(II)alamin, it is assumed that the influence of the $\mathrm{Co^{II}}$−organic radical spin−spin interaction on the ESEEM frequencies and intensities can be neglected for microwave excitation at $g = 2.3$ (*14*). After deletion of the early envelope modulation segment corresponding to the deadtime in the experimental envelope modulation, deadtime reconstruction was performed (*60*) and the envelope modulation was Fourier transformed to obtain the simulated ESEEM frequency spectrum, as in the analysis of the experimental envelope modulation. To facilitate the comparison between experimental and simulated ESEEM, the simulated modulation envelopes were multiplied by exponential decay functions derived from regression fitting of the modulation decay in the experimental envelopes. The simulations and analysis were performed with routines written by using Matlab (Mathworks, Nantick, MA) and run on Silicon Graphics Indigo2 or PowerMacintosh computers.

In the ESEEM simulations, the variable input parameters include: the diagonal hyperfine tensor components, $[A_\perp, A_\perp, A_\parallel]$, which are the sum of an isotropic component (A_{iso}) and the point dipolar tensor components, $[-A_{\mathrm{dip}}, -A_{\mathrm{dip}}, 2A_{\mathrm{dip}}]$, where $A_{\mathrm{dip}} = g_e\beta_e g_n\beta_n\, h^{-1}\, r^{-3}$ (MHz), nuclear quadrupole interaction parameters representing the magnitude (e^2qQ) and the asymmetry (η) of the electric field gradient at the nitrogen nucleus, and Euler angles, [α, β, γ], which define the mutual orientation of the electric field gradient tensor and hyperfine tensor principal axes. The free electron and nuclear frequencies are fixed by the experimental magnetic field value. ESEEM simulated for individual ^{14}N nuclei were combined to produce the composite ESEEM in accord with the product rule (*59*). The parameters were adjusted manually, and the best overall ("global") match of the simulated and experimental time and frequency domain data for the range of τ and magnetic field values employed was determined visually. The limits on the parameter values in Table 1 represent values that, if exceeded, lead to significantly poorer simulation of the experimental data.

Ab Initio/Density Functional Computations. The description of the test calculations and procedures for computation of ^{14}N nuclear quadrupole parameters for ligand model compounds has been described in detail by Torrent et al. (*50*). In brief, full geometry optimization of axial ligand molecule models was carried out at the B3LYP/6-311G** level. The PW91P86/6-311++G(2d,2p) level was selected for evaluation of one-electron properties. Long-range solvent effects were included by using a polarizable dielectric model (*65*−*67*) incorporating a dielectric constant of 78.39, appropriate for aqueous solution. All calculations were carried out with the Gaussian 98 package.

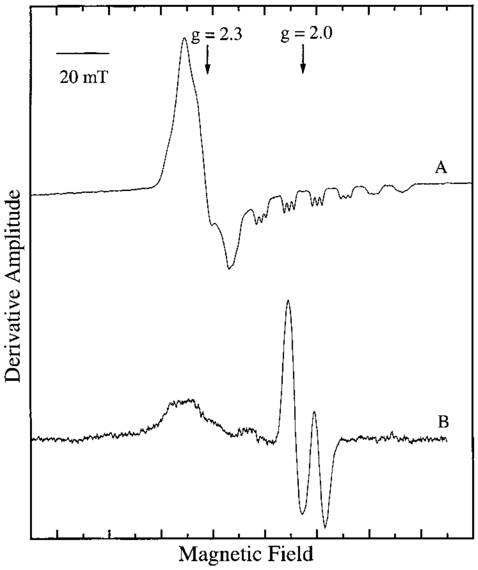

FIGURE 2: EPR spectra of free cob(II)alamin cryotrapped in glycerol−water glass and cob(II)alamin formed in ethanolamine deaminase and cryotrapped under conditions of steady-state turnover: (A) base-on cob(II)alamin, pH 7.0; (B) cob(II)alamin in ethanolamine deaminase. The doublet line shape around $g = 2$ arises from the substrate radical. Conditions: microwave power, 4 mW; microwave frequency, 9.45 GHz; magnetic field modulation, 1.0 mT; modulation frequency, 100 kHz; temperature, 100 K; average of 4−8 scans minus baseline.

RESULTS

EPR Spectroscopy. Figure 2A displays the X-band continuous-wave EPR spectrum of free cob(II)alamin in the base-on (pH 7.0) state in low-temperature 1:1 glycerol−aqueous glass. This spectrum is similar to that reported previously for base-on cob(II)alamin (*42*). Equatorial coordination by the slightly distorted square planar (*18*) array of corrin ring nitrogen atoms gives rise to an axially symmetric EPR line shape, with zero-crossing of the $g_\perp$ feature at $g = 2.3$. The spectrum shows an eight-line pattern with a splitting of 10.7 mT centered at $g_\parallel = 2.0$ that is caused by coupling of the unpaired electron in the $\mathrm{Co^{II}}$ d_{z^2} orbital with the cobalt nucleus (cobalt nuclear spin, $I = {}^7/_2$). The cobalt hyperfine splitting is not resolved at $g_\perp$ (*42*). The d_{z^2} electron is also relatively strongly coupled to the proximal ^{14}N nucleus (^{14}N nuclear spin, $I = 1$) of dimethylbenzimidazole, which results in a superhyperfine splitting (1.9 mT) of each member of the octet into a triplet. The superhyperfine splitting is typically resolved in only the low-field hyperfine features (*42*). No other superhyperfine couplings are resolved in the EPR spectrum owing to inhomogeneous broadening.

Figure 2B shows that the biradical EPR spectrum obtained by cryotrapping *S. typhimurium* ethanolamine deaminase during steady-state turnover on the substrate, 2-aminopropanol, is dramatically different from the free base-on cob(II)alamin spectrum. The spectrum features a doublet line shape in the $g = 2$ region that arises from transitions nominally associated with the substrate radical. The doublet splitting of the radical is caused by electron spin−spin exchange and dipolar interactions between the substrate

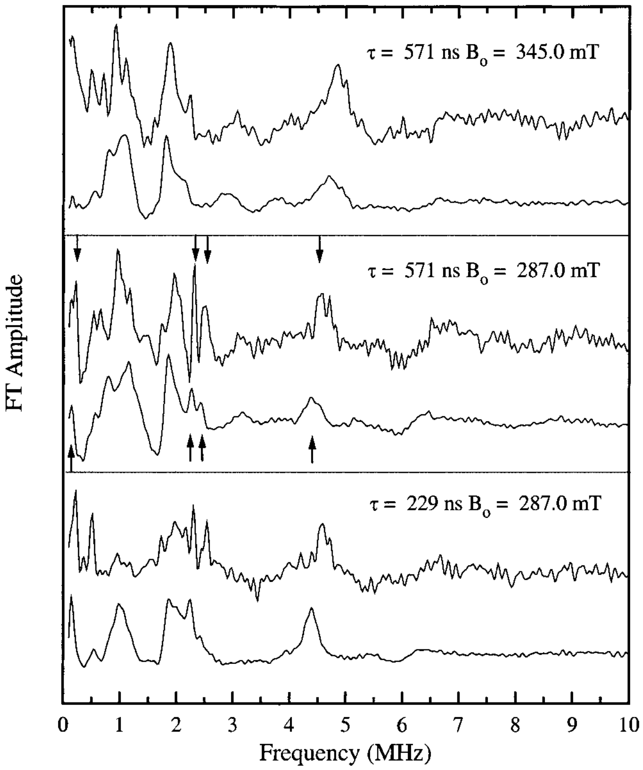

FIGURE 3: Three-pulse ESEEM spectra of cob(II)alamin cryotrapped in the free base-on form in glycerol−water glass (bottom spectrum in panel) and formed in ethanolamine deaminase and cryotrapped under conditions of steady-state turnover (top spectrum in each panel). The features assigned to the N1 nitrogen of dimethylbenzimidazole in the free (upward arrows) and enzyme-bound (downward arrows) states are indicated. Each panel presents data obtained at the indicated τ and magnetic field value. At the magnetic field (B_0) value of 287.0 mT, the microwave frequency was adjusted to 8.841 and 8.926 GHz for the free base-on and enzyme-bound cob(II)alamin, respectively, so that the data could be obtained at $g_\perp$ for each sample. For B_0 = 345.0 mT, the microwave frequencies were 10.718 and 10.726 GHz for free base-on and enzyme-bound cob(II)alamin, respectively. Conditions: temperature, 6 K; microwave pulse power, 20 W; initial $\tau + T$ value, 200 ns; pulse width, 20 ns; pulse repetition rate, 16 Hz; 16 repetitions averaged per point.

radical and Co^{II} over a separation distance of 10−12 Å (*43*). The broad feature centered at approximately g = 2.3 arises from the $g_\perp$ region of Co^{II} in the biradical. The line shape of Co^{II} is distorted by the biradical interaction, so that no cobalt hyperfine or nitrogen superhyperfine splittings are resolved. The status of Co^{II} ligation in enzyme-bound cob(II)alamin in the Co^{II}−substrate biradical catalytic intermediate can therefore not be determined from the EPR spectrum.

ESEEM Spectroscopy. Free Cob(II)alamin. Figure 3 shows three-pulse ESEEM spectra obtained for base-on cob(II)alamin trapped in the low-temperature glycerol−water glass. ESEEM was collected in the $g_\perp$ region at the g-value corresponding to maximum ESE intensity. The ESEEM spectra show features in the frequency region below 5 MHz. The low-frequency values and shifts in position by ≤0.2 MHz upon change of the magnetic field from 287.0 to 345.0 mT (^{1}H features would shift by 2.5 MHz over this range) are characteristic of features arising from superhyperfine coupling of Co^{II} to the low nuclear g-value (g_n = 0.4034) ^{14}N nucleus [free nuclear frequency, 0.89 MHz (at B_0 = 287.0 mT) and 1.07 MHz (at B_0 = 345.0 mT)].

A set of narrow features positioned at 0.2, 2.3, and 2.5 MHz are apparent in the base-on cob(II)alamin ESEEM spectra obtained at 287.0 mT and are shown in Figure 3 by the upward-pointing arrows. This pattern, where the sum of the two lower frequencies is equal to the third, is characteristic of ^{14}N coupling when the hyperfine and nuclear Zeeman contributions are equal and oppositely signed for one electron spin manifold ($A/2 = \nu_N$, where ν_N is the free nuclear frequency). This creates a zero-field, or "exact cancellation", condition (*46*, *48*), in which the energy level separation for one m_s state is determined by the nuclear quadrupole interaction. The lines are narrow because the nuclear quadrupole interaction is not influenced by magnetic field anisotropy. Small deviations from exact cancellation, owing to a mismatched isotropic hyperfine and nuclear Zeeman coupling, or to a significant ^{14}N dipolar hyperfine interaction, introduce line broadening and some frequency position dependence of the spectral features on the external magnetic field strength. A fourth spectral feature is also characteristic of the exact cancellation condition (*46*, *48*). This "double quantum" feature arises from the $\Delta m_I = \pm 2$ splitting in the m_s manifold in which the hyperfine and nuclear Zeeman contributions add, and is observed at 4.4 MHz in spectra obtained at 287.0 mT. Figure 3 shows that the double quantum feature is maintained in ESEEM at the higher magnetic field value of 345.0 mT but that the nuclear quadrupole-dominated features are severely attenuated. This may be caused, in part, by the magnetic field-induced shift away from the exact cancellation condition for some of the Co^{II}−^{14}N isochromats and by magnetic field-dependent increases in the modulation depth arising from other coupled ^{14}N nuclei.

Figure 3 shows additional ESEEM spectral features arising from coupling of the unpaired electron with other ^{14}N nuclei. At all τ values examined, features are centered at 1.0 and 1.8 MHz, with intensity at 0.5 MHz at some τ values. These features represent another set of one or more nitrogen nuclei that are coupled to Co^{II}. The comparable values of the sum of the two lower frequencies (1.5 MHz) and the third frequency value (1.8 MHz) indicates that the Co^{II}−^{14}N superhyperfine coupling also approximates this exact cancellation condition, although the τ- and magnetic field-dependence of the line shape suggest a more significant anisotropic dipolar contribution and mismatch of the isotropic hyperfine and ^{14}N nuclear Zeeman coupling energies than for the Co^{II}−^{14}N interaction described above.

Ethanolamine Deaminase-Bound Cob(II)alamin. Figure 3 also shows three-pulse ESEEM spectra obtained for cob(II)alamin bound to ethanolamine deaminase in the Co^{II}−substrate biradical state. The enzyme-bound data were obtained at the same resonant magnetic fields and position of microwave pulse excitation (at $g_\perp$) as for the corresponding free cob(II)alamin data. This was facilely accomplished with the broad band pulsed-EPR spectrometer by adjusting the microwave frequency. A significant difference between the two spectra is the enhanced spectral resolution for enzyme-bound cob(II)alamin. This may reflect dispersion of the free cob(II)alamin conformation in the glass, relative to a discrete conformation in the enzyme. Enhanced resolution of the cobalt hyperfine and proximal nitrogen superhyperfine features has been previously noted in EPR spectra of ribonucleotide triphosphate reductase-bound cob(II)alamin

(*42*, *68*). As shown by the downward-pointing arrows in Figure 3, the set of features observed at 0.2, 2.3, 2.5, and approximately 4 MHz for free cob(II)alamin is also present in ESEEM from enzyme-bound cob(II)alamin. The nuclear quadrupole features are shifted by <0.1 MHz and the frequency position of the double quantum feature is increased by 0.2−0.3 MHz in the enzyme-bound relative to the free state of cob(II)alamin. These results show that the ^{14}N nucleus that gives rise to this set of features is coupled to Co^{II} in both free and ethanolamine deaminase-bound cob(II)alamin.

Figure 3 shows that the ESEEM intensity centered at 0.5, 1.0, and 1.8 MHz in free cob(II)alamin is also present in the ethanolamine deaminase-bound state. The similar frequency positions and roughly comparable line shapes suggest that these features arise from one or more ^{14}N that are coupled in common to Co^{II} in free and ethanolamine deaminase-bound cob(II)alamin.

Cobinamide−Ligand Complexes. The most likely origins of the ^{14}N features in the ESEEM spectra of cob(II)alamin are the four equatorial nitrogen ligands at the inner edge of the corrin ring and the nitrogens of the axial ligand. To assist in distinguishing the corrin and axial ligand nitrogen contributions to the cob(II)alamin ESEEM spectra, ESEEM was collected under comparable conditions for cob(II)inamide model complexes with either 1-methylbenzimidazole or imidazole as axial ligand. 1-Methylbenzimidazole is a model for the 1-ribosyl-5,6-dimethylbenzimidazole ligand in intact cob(II)alamin, while imidazole models the histidine-based axial ligand that has been identified for cob(II)alamin in methylcobalamin-dependent methionine synthase (*26*, *27*) and carbon skeleton-rearranging adenosylcobalamin-dependent enzymes (*28*−*30*). The continuous-wave EPR spectra of these complexes are comparable to the spectrum of free base-on cob(II)alamin presented in Figure 2A. (The EPR and ESEEM characterization of these and related Co^{II}−ligand complexes will be described in detail in a separate report: S.-C. Ke and K. Warncke, manuscript in preparation.) To a first approximation, we assume that the corrin ring ^{14}N contributions to the ESEEM are comparable in the two model complexes. Therefore, large differences in the ESEEM between the two complexes are attributed to changes in the ESEEM from ^{14}N in the axial ligand.

Figure 4 shows ESEEM spectra obtained for the cob(II)inamide complexes with 1-methylbenzimidazole and imidazole as axial ligands. The spectra differ substantially. The spectrum for cob(II)inamide−imidazole displays prominent features at 0.47, 1.01 1.55, and 3.90 MHz that are not present in the ESEEM spectrum obtained from the cob(II)inamide−1-methylbenzimidazole complex. The cob(II)inamide−1-methylbenzimidazole spectrum shows a unique feature positioned at 0.14 MHz and an apparent increase and sharpening of the spectral amplitude at 2 MHz. The feature at 4.25 MHz is also larger in the cob(II)inamide−1-methylbenzimidazole spectrum. To attenuate spectral contributions from coupled ^{14}N in the corrin ring, and thus to emphasize features arising from the ^{14}N of the axial ligands, the ^{14}N ESEEM for the two ligands was envelope-divided (*47*, *69*, *70*). The resulting cob(II)inamide−1-methylbenzimidazole/cob(II)inamide−imidazole quotient ESEEM is shown in Figure 4C. The dominant positive features at 0.14, 1.98, 2.14, and 4.22 MHz are assigned to nitrogen in the 1-methylbenzimidazole ligand. Negative features at 0.53, 1.02, 1.51, and 3.86 MHz are assigned to ^{14}N in the imidazole ligand.

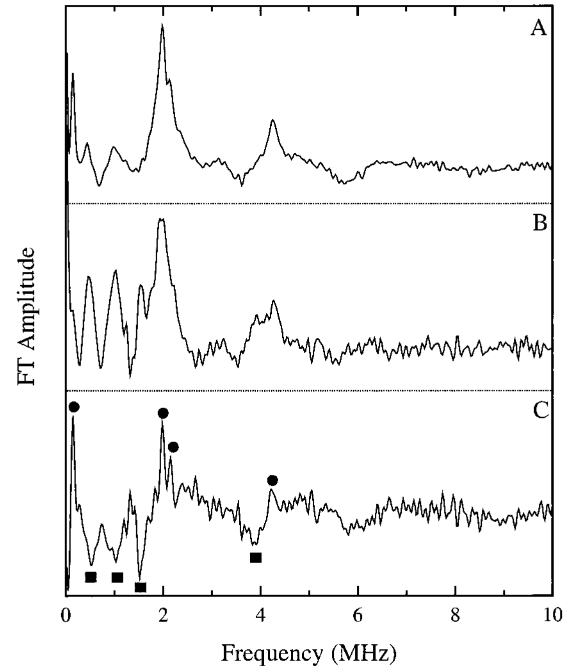

FIGURE 4: Three-pulse ESEEM spectra of cob(II)inamide−ligand complexes cryotrapped in glycerol−water glass: (A) cob(II)inamide−1-methylbenzimidazole; (B) cob(II)inamide-imidazole; (C) cob(II)inamide−1-methylbenzimidazole/cob(II)inamide−imidazole quotient ESEEM spectrum. The features from N1 of 1-methylbenzimidazole (circles) and imidazole (squares) are indicated. Conditions: τ, 212 ns; magnetic field strength, 289.6 mT; microwave frequency, 9.01−9.03 GHz; temperature, 6 K; microwave pulse power, 20 W; initial $\tau + T$ value, 200 ns; pulse width, 20 ns; pulse repetition rate, 16 Hz; 16 repetitions averaged per point. Spectra A and B were obtained from the average of 5 and 8 individual envelopes, respectively.

DISCUSSION

Spectral Assignments. Axial Ligand Nitrogen in Free Cob(II)alamin. The set of ^{14}N features at 0.14, 1.98, 2.14, and 4.22 MHz in the ESEEM spectrum from the cob(II)inamide−1-methylbenzimidazole complex in Figure 4 correspond closely with the features observed in free cob(II)alamin at 0.2, 2.3, 2.5, and 4.4 MHz shown in Figure 3. In contrast, these features are absent in ESEEM spectra from the cob(II)inamide−imidazole complex. The proximal N3 nitrogen atom is not expected to contribute to the ESEEM, because the ^{14}N superhyperfine isotropic coupling of 47.5 MHz and the low dipolar anisotropy ($A_{\mathrm{dip}} = 2.5$ MHz) (*71*) shifts the couplings beyond the ESEEM frequency window and severely limits the superposition of nuclear states that is required for observation of ESEEM (*64*). Therefore, the set of ^{14}N features at 0.2, 2.3, 2.5, and 4.4 MHz (at 287.0 mT) in the ESEEM spectra of free cob(II)alamin are assigned to the remote nitrogen nucleus (N1) of the dimethylbenzimidazole axial ligand.

Axial Ligand Nitrogen in Ethanolamine Deaminase-Bound Cob(II)alamin. There is a striking correspondence between the set of ^{14}N features at 0.2, 2.3, 2.5, and 4.4 MHz that are assigned to the N1 nitrogen of dimethylbenzimidazole in free cob(II)alamin and the features at 0.2, 2.2, 2.4, and 4.8 MHz in the enzyme-bound cob(II)alamin ESEEM spectra. There is also a strong dissimilarity between the ESEEM spectrum of the cob(II)inamide−imidazole complex presented in Figure 4 and the spectra of ethanolamine deaminase-bound cob(II)alamin presented in Figure 3. Thus, the axial ligand in cob(II)alamin bound to ethanolamine deaminase during steady-state turnover is dimethylbenzimidazole. We propose that dimethylbenzimidazole is also the axial ligand to the coenzyme in the resting state of the enzyme.

Corrin Ring Equatorial Ligand Nitrogen. The features centered at 0.5, 1.0, and 1.8 MHz in the spectra of Figure 3 are assigned to the corrin ring ^{14}N nuclei that comprise the equatorial ligation field of Co^{II}. This assignment is supported by the positions of the nuclear quadrupole-dominated features from the pyrrole nitrogen nuclei in ESEEM spectra of Co^{II}−tetraphenylporphyrin (Co^{II}−TPP) complexes (0.6, 1.2, and 1.7 MHz with pyridine as axial ligand: K. Warncke and S.-C. Ke, manuscript in preparation). In addition, frequency positions of features from equatorially liganding pyrrole nitrogen nuclei in dioxygen−Co^{II}−TPP−ligand complexes have been observed at 0.5, 1.1, and 1.6 MHz (*72*). Although the overall structures of the corrin and porphyrin ring systems are substantially different, the pyrrole nitrogen nuclei in TPP are approximate magnetic and nuclear quadrupole interaction models for the corrin ring nitrogen nuclei. We also considered the possibility that the features at 0.5, 1.0, and 1.8 MHz arose from coupling to one or more ^{14}N in the amide side chains of cob(II)alamin. As shown in Figure 1, there are three acetamide and three propionamide primary amide side chains and one secondary amide in the nucleotide tail. However, the amide nitrogens are removed from Co^{II} by at least six covalent bonds, and there is no formal conjugation between these nitrogen atoms and the inner corrin ring. Unlike the pyrrole rings in porphyrins, which are fully conjugated, the five-membered rings in the corrin structure are only conjugated along the inner edge of the macrocycle. We therefore rule out the amide nitrogens as sources of the ^{14}N ESEEM.

ESEEM Simulations. N1 Nitrogen of Dimethylbenzimidazole. An independent method of identifying the chemical origin of ^{14}N ESEEM in the near exact cancellation limit is to compare the nuclear quadrupole parameters obtained from ESEEM simulations with parameters obtained for ^{14}N nuclei in known, chemically comparable compounds. This is because the nuclear quadrupole coupling constant, e^2qQ, and electric field gradient asymmetry parameter, η, are characteristic of the chemical type of ^{14}N nuclei (*73, 74*). Figure 5 shows representative experimental and corresponding simulated ESEEM spectra for cryotrapped free base-on cob(II)alamin and ethanolamine deaminase-bound cob(II)alamin. The Co^{II}−^{14}N superhyperfine and ^{14}N nuclear quadrupole coupling parameters that best simulate the τ- and magnetic field-dependence of the set of features assigned to the coupled N1 nucleus in free and ethanolamine deaminase-bound cob(II)alamin are presented in Table 1.

Figure 3 shows that the double quantum feature is increased by 0.2−0.3 MHz when cob(II)alamin is bound in ethanolamine deaminase (downward arrow) relative to free in solution (upward arrow). The simulation parameters in Table 1 show that the shift arises primarily from an increase in the A_{iso} value in the enzyme-bound state of cob(II)alamin. The increase in A_{iso} shows that a larger amount of unpaired spin density is delocalized from Co^{II} onto dimethylbenzimidazole when cob(II)alamin is enzyme-bound relative to free in solution.

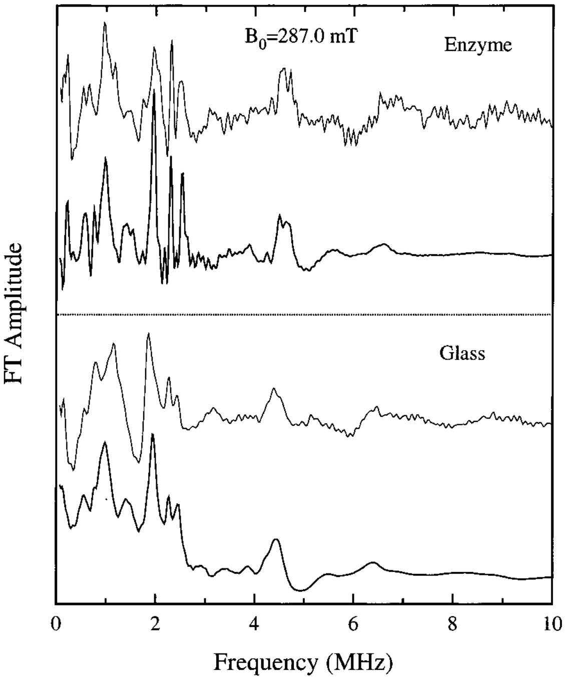

FIGURE 5: Three-pulse ^{14}N ESEEM simulations for cob(II)alamin in the free base-on form in glycerol−water glass and bound in ethanolamine deaminase under conditions of steady-state turnover. The simulated spectra are shown in bold at the bottom of each panel, with the corresponding experimental spectra at the top of each panel. The spectra correspond to a common τ value of 571 ns and B_0 value of 287.0 mT. The simulation parameters are presented in Table 1 and described in the text. Experimental parameters are given in Figure 3.

Corrin Ring Equatorial Ligand Nitrogen. The simulation parameters for N1 are determined with high accuracy, because the superhyperfine coupling with this nucleus is very near to exact cancellation. This gives sharp, minimally τ- and magnetic field strength-dependent (in the X-band frequency range) features that offer a well-defined target for reproduction. In contrast, the simulation of the ESEEM assigned to the corrin ring ^{14}N nuclei is challenging, because of broadening of the line shapes caused by a significant dipolar hyperfine interaction, overlapping transitions from possible slight inequivalence in the Co^{II}−^{14}N superhyperfine and ^{14}N nuclear quadrupole coupling of each nucleus, contributions from four nuclei which can include harmonics of the fundamental frequencies (*75*), and the lack of a strong “double quantum” feature. Our efforts to simulate the corrin ^{14}N ESEEM have not yet converged. Nevertheless, it is important to include the corrin ring ^{14}N coupling in the ESEEM simulations, so that the modulation depth of the N1 contribution is properly scaled. Therefore, a provisional set of simulation parameters (A_{iso} = 1.7 MHz, r_{eff} = 2.2 Å, e^2qQ = 1.8 MHz, η = 0.85) were used to approximate the corrin ring ^{14}N features, and the results are displayed in Figure 5. The relatively large η value may reflect inequivalence in ESEEM from the different corrin ^{14}N. This parameter set was based on pyrrole ^{14}N nuclear quadrupole coupling parameters estimated from our own ESEEM results for Co^{II}−TPP−ligand complexes (e^2qQ = 2.0 MHz, η =0.4) (Ke, S.-C. and Warncke, K., manuscript in preparation) and in dioxygen−Co^{II}−TPP−ligand complexes (*72*). With the inclusion of the four coupled corrin ring ^{14}N, the relative amplitude of the N1 contribution to the ESEEM is obtained with a single coupled ^{14}N nucleus. This is in agreement with the assignment of the N1 features.

Computation of the N1 Nuclear Quadrupole Coupling Parameters. The typing of the coupled ^{14}N nucleus by using nuclear quadrupole parameters determined by ESEEM simulations relies on values determined independently for known compounds. Experimentally determined nuclear quadrupole parameters for 1-methylbenzimidazole and 1-alkyl-5,6-dimethylbenzimidazole compounds are not available in the literature. In addition, literature values of e^2qQ and η for different types of ^{14}N have been largely determined in the gas phase or in molecular crystals (*73*, *74*). While the crystal environment may reasonably model the density and electrostatic interactions in a protein interior, it may not necessarily reproduce the environment in aqueous medium. Therefore, the nuclear quadrupole parameters for the 1-methylbenzimidazole and 1,5,6-trimethylbenzimidazole models for the axial ligands have been computed by using density functional theory (DFT) with the inclusion of a polarizable dielectric model of long-range aqueous solvent effects (*49*).

The density functional calculations give values of 3.073 MHz and 0.111 for e^2qQ and η, respectively, for N1 in 1,5,6-trimethylbenzimidazole, in very good agreement with the values of $e^2qQ = 3.20$ (3.12) MHz and $\eta = 0.12$ (0.07) obtained by the ESEEM simulations of the set of features assigned to N1 in free (enzyme-bound) cob(II)alamin. The calculated values of e^2qQ and η for N1 in 1-*N*-methylbenzimidazole are 2.992 MHz and 0.098, respectively. The comparable parameters calculated for 1-methylbenzimidazole and 1,5,6-trimethylbenzimidazole agree well with the modest difference between the N1 features in the ESEEM from the cobinamide−1-methylbenzimidazole complex and cob(II)alamin. In addition, distinctly different values of $e^2qQ = 2.097$ and $\eta = 0.229$ are obtained for the amine nitrogen in imidazole, which would produce N1 ESEEM significantly different from that observed for cob(II)alamin. The ESEEM simulation/DFT computation approach provides an independent route to assignment of the ESEEM spectral features to the N1 nitrogen of dimethylbenzimidazole, and therefore, the demonstration that dimethylbenzimidazole is the axial ligand to cob(II)alamin in ethanolamine deaminase.

Implications for Vitamin B_{12} Coenzyme Function in Ethanolamine Deaminase. We have provided the first evidence that dimethylbenzimidazole is the axial ligand to Co^{II} in cob(II)alamin bound to ethanolamine deaminase. Ethanolamine deaminase thus joins diol dehydrase (*37*) and ribonucleotide triphosphate reductase (*38*) as a member of the heteroatom-eliminating, class II vitamin B_{12} coenzyme-dependent enzymes whose α-axial ligands have been directly determined to be dimethylbenzimidazole. Our direct determination is the only one thus far performed on active enzyme in a catalytic intermediate state. The results show directly that cob(II)alamin is a pentacoordinate, α-axial-liganded complex during catalysis, contrary to a previous controversial proposal (*76*). The presence of the dimethylbenzimidazole ligand to cob(II)alamin also indicates that the mechanochemical model proposed (*19*−*25*) for cobalt−carbon bond weakening by compression of the Co^{II}−N3 bond is viable in ethanolamine deaminase. The axial dimethylbenzimidazole coordination in situ is consistent with the absence in *S. typhimurium* ethanolamine deaminase (*33*) of the consensus sequence that is characteristic of carbon skeleton-rearranging, class I enzymes that use histidine imidazole as the α-axial ligand (*26*, *31*, *32*). The mechanistic basis for the different α-axial ligands is not yet apparent (*16*).

The results also show that ESEEM spectroscopy is a sensitive probe of the electronic structure of cob(II)alamin. The 0.2−0.3 MHz increase in the value of the double quantum feature for the Co^{II}−N1 coupling in free cob(II)alamin relative to the cob(II)inamide−1-methylbenzimidazole complex suggests that the dimethylbenzimidazole ligand is not completely free to minimize its free energy of interaction with Co^{II} and, therefore, that the nucleotide loop exercises some control over the Co^{II}−axial ligand interaction in free cob(II)alamin. This result is in agreement with proposals for the presence of strain in the nucleotide loop (*77*, *78*), but counter to the opposing view (*79*).

The further 14% increase in the isotropic hyperfine coupling of the remote dimethylbenzimidazole ^{14}N nucleus in enzyme-bound versus free cob(II)alamin indicates that the interaction with the protein causes an enhanced delocalization of unpaired spin density from Co^{II} onto the axial ligand. A discrete binding mode for cob(II)alamin in ethanolamine deaminase, suggestive of strong, specific interactions with the protein, is evinced by the enhanced ESEEM spectral resolution from the enzyme-bound relative to free solution cob(II)alamin. The removal of unpaired spin density by the axial base would contribute to the acceleration of cobalt−carbon bond cleavage in situ by reducing the radical character on Co^{II}, which would defeat the recombination reaction. This interpretation is consistent with the substrate radical−Co^{II} biradical state examined in these studies, which might be expected to reveal protein-induced changes in cob(II)alamin structure that enhance the radical pair yield. We are examining the structure of cob(II)alamin in the recently identified (*14*, *15*) product radical−Co^{II} biradical state, where adjustment of the cob(II)alamin structure to favor re-formation of the cobalt−carbon bond may be developing.

ACKNOWLEDGMENT

The use of the computational facilities at the Emerson Center (Emory University) is acknowledged. M.T. acknowledges a Postdoctoral Fullbright Fellowship from the Ministerio de Educacion y Cultura of Spain. We are grateful to Ms. Jenna Trommel and Professor Luigi Marzilli (Department of Chemistry, Emory University) for the gift of methylcobinamide.

REFERENCES

1. Babior, B. M., and Krouwer, J. S. (1979) *CRC Crit. Rev. Biochem.* 35−102.
2. *B12* (1982) (Dolphin, D., Ed.) Vols. 1 and 2, Wiley, New York.
3. Frey, P. (1990) *Chem. Rev. 90*, 1343−1357.
4. Buckel, W., and Golding, B. T. (1996) *Chem. Soc. Rev. 25*, 329−338.
5. Stubbe, J., and van der Donk, W. A. (1998) *Chem. Rev. 98*, 705−762.
6. Marsh, E. N. G. (1995) *Biochemistry 34*, 7542−7547.
7. Gerfen, G. J., Licht, S., Willems, J.-P., Hoffman, B. M., and Stubbe, J. (1996) *J. Am. Chem. Soc. 118*, 8192−8197.
8. Licht, S., Gerfen, G. J., and Stubbe, J. (1996) *Science 271*, 477−481.

9. O'Brien, R. J., Fox, J. A., Kopczynski, M. G., and Babior, B. M. (1985) *J. Biol. Chem. 260*, 16131−16136.
10. Finke, R. G., and Hay, B. P. (1984) *Inorg. Chem. 23*, 3041−3043.
11. Finke, R. G., and Hay, B. P. (1985) *Inorg. Chem. 24*, 1278.
12. Padmakumar, R., Padmakumar, R., and Banerjee, R. (1997) *Biochemistry 36*, 3713−3718.
13. Marsh, E. N. G., and Ballou, D. P. (1998) *Biochemistry 37*, 11864−11872.
14. Ke, S.-C., and Warncke, K. *J. Am. Chem. Soc.* (in press).
15. Warncke, K., Schmidt, J. C., and Ke, S.-C. *J. Am. Chem. Soc.* (submitted for publication).
16. Garr, C. D., Sirovatka, J. M., and Finke, R. G. (1996) *Inorg. Chem. 35*, 5912−5922.
17. Brown, K. L., and Li, J. (1998) *J. Am. Chem. Soc. 120*, 9466−9474.
18. Glusker, J. P. (1982) in *B12* (Dolphin, D., Ed.) Vol. 1, pp 23−106, Wiley, New York.
19. Kräutler, B., Keller, W., and Kratky, C. (1989) *J. Am. Chem. Soc. 111*, 8936−8938.
20. Grate, J. H., and Schrauzer, G. N. (1979) *J. Am. Chem. Soc. 101*, 4601.
21. Schrauzer, G. N., and Grate, J. H. (1981) *J. Am. Chem. Soc. 103*, 541.
22. Bresciani-Pahor, N., Forcolin, M., Marzilli, L. G., Randaccio, L., Summers, M. F., and Toscano, P. J. (1985) *Coord. Chem. Rev. 63*, 1.
23. Marzilli, L. G., Summers, M. F., Bresciani-Pahor, N., Zangrando, E., Charland, J.-P., and Randaccio, L. (1985) *J. Am. Chem. Soc. 107*, 6880.
24. Marzilli, L. G. (1993) in *Bioinorganic Catalysis* (Reedjik, J., Ed.) Marcell Dekker, New York.
25. Krautler, B., Konrat, R., Stupperich, E., Faber, G., Gruber, K., and Kratky, C. (1994) *Inorg. Chem. 33*, 4128.
26. Drennan, C. L., Huang, S., Drummond, J. T., Matthews, R. G., and Ludwig, M. L. (1994) *Science 266*, 1669−1674.
27. Ludwig, M. L., and Matthews, R. G. (1997) *Annu. Rev. Biochem. 66*, 269−313.
28. Padmakumar, R., Taoka, S., Padmakumar, R., and Banerjee, R. (1995) *J. Am. Chem. Soc. 117*, 7033−7034.
29. Mancia, F., Keep, N. H., Nakagawa, A., Leadlay, P. F., McSweeney, S., Rasmussen, B., Bösecke, P., Diat, P., and Evans, P. R. (1996) *Structure 4*, 339−350.
30. Zelder, O., Beatrix, B., Kroll, F., and Buckel, W. (1995) *FEBS Lett. 369*, 252−254.
31. Marsh, E. N. G., and Holloway, D. E. (1992) *FEBS Lett. 310*, 167−170.
32. Beatrix, B., Zelder, O., Linder, D., and Buckel, W. (1994) *Eur. J. Biochem. 221*, 101−109.
33. Faust, L. P., Connor, J. A., Roof, D. M., Hoch, J. A., and Babior, B. M. (1990) *J. Biol. Chem. 265*, 12462−12466.
34. Booker, S., and Stubbe, J. (1993) *Proc. Natl. Acad. Sci. U.S.A. 90*, 8352−8356.
35. Tobimatsu, T., Azuma, M., Matsubara, H., Takatori, H., Niida, T., Nishimoto, K., Satoh, H., Hayashi, R., and Toraya, T. (1996) *J. Biol. Chem. 271*, 22352−22357.
36. Seyfried, M., Daniel, R., and Gottschalk, G. (1996) *J. Bacteriol. 178*, 5793−5796.
37. Yamanishi, M., Yamada, S., Muguruma, H., Murakami, Y., Takamasa, T., Ishida, A., Yamauchi, J., and Toraya, T. (1998) *Biochemistry 37*, 4799−4803.
38. Lawrence, C. C., Gerfen, G. J., Samano, V., Nitsche, R., Robins, M., Retey, J., and Stubbe, J. (1999) *J. Biol. Chem. 274*, 7039−7042
39. Babior, B. M. (1982) in *B12* (Dolphin, D., Ed.) Vol. 2, pp 263−288, Wiley, New York.
40. Faust, L. P., and Babior, B. M. (1992) *Arch. Biochem. Biophys. 294*, 50−54.
41. Babior, B. M., Moss, T. H., Orme-Johnson, W. H., and Beinert, H. (1974) *J. Biol. Chem. 249*, 4537−4544.
42. Pilbrow, J. (1982) in *B12* (Dolphin, D., Ed.) Vol. 1, pp 431−462, Wiley, New York.
43. Boas, J. F., Hicks, P. R., and Pilbrow, J. R. (1978) *J. Chem. Soc., Faraday 2, 74*, 417.
44. Kevan, L., and Bowman, M. K. (1990) *Modern Pulsed and Continuous Wave Electron Spin Resonance*, Wiley, New York.
45. Schweiger, A. (1991) *Angew. Chem., Int. Ed. Engl. 30*, 265−292.
46. Mims, W. B., and Peisach, J. (1978) *J. Chem. Phys. 69*, 4921−4930.
47. Mims, W. B., and Peisach, J. (1989) in *Advanced EPR: Applications in Biology and Chemistry* (Hoff, A. J., Ed.) pp 1−57, Elsevier, New York.
48. Flanagan, H. L., and Singel, D. J. (1987) *J. Chem. Phys. 87*, 5606.
49. Torrent, M., Musaev, D. G., Ke, S.-C., Warncke, K. and Morokuma, K. *J. Phys. Chem. B* (submitted for publication).
50. Ladd, J. N., Hogenkamp, H. P. C., and Barker, H. A. (1961) *J. Biol. Chem. 236*, 2114−2118.
51. Pratt, J. M. (1982) in *B12* (Dolphin, D., Ed.) Vol. 1, pp 325−392, Wiley, New York.
52. Harkins, T. T., and Grissom, C. B. (1995) *J. Am. Chem. Soc. 117*, 566−567.
53. Babior, B. M., and Li, T. K. (1969) *Biochemistry 8*, 154−160.
54. Bartos, J., and Pesez, M. (1979) *Pure Appl. Chem. 51*, 1803−1814.
55. Britt, R. D., and Klein, M. P. (1987) *J. Magn. Reson. 74*, 535−540.
56. Lin, C. P., Bowman, M. K., and Norris, J. R. (1985) *J. Magn. Reson. 65*, 396−374.
57. Fauth, J. M., Schweiger, A., Braunschweiler, L., Forrer, J., and Ernst, R. R. (1986) *J. Magn. Reson. 66*, 74−86.
58. Fauth, J. M., Schweiger, A., and Ernst, R. R. (1989) *J. Magn. Reson. 81*, 262−274.
59. Mims, W. B. (1972b) *Phys. Rev. B 6*, 3543−3545.
60. Mims, W. B. (1984) *J. Magn. Reson. 59*, 291−306.
61. Abragam, A., and Bleaney, B. (1986) *Electron Paramagnetic Resonance of Transition Ions*, pp 133−178, Dover, New York.
62. Hutchison, C. A., and McKay, D. B. (1977) *J. Chem. Phys. 66*, 3311.
63. Hurst, G. C., Henderson, T. A., and Kreilick, R. W. (1985) *J. Am. Chem. Soc. 107*, 7294−7299.
64. Mims, W. B. (1972) *Phys. Rev. B 5*, 2409−2419.
65. Miertus, S., Scrocco, E., and Tomasi, J. (1981) *Chem. Phys. 55*, 117.
66. Miertus, S., and Tomasi, J. (1982) *Chem. Phys. 65*, 239.
67. Cossi, M., Barone, R., Cammi, R., and Tomasi, J. (1996) *Chem. Phys. Lett. 255*, 327.
68. Hamilton, J. A., Blakley, R. L., Looney, F. D., and Winfield, M. E. (1969) *Biochim. Biophys. Acta 177*, 374.
69. Warncke, K., Brooks, H. B., Babcock, G. T., Davidson, V. L., and McCracken, J. (1993) *J. Am. Chem. Soc. 115*, 6464−6565.
70. Warncke, K., and McCracken, J. (1995) *J. Chem. Phys. 103*, 6829−6840.
71. Jorin, E., Graf, F., Schweiger, A., and Günthard, Hs. H. (1976) *Chem. Phys. Lett. 42*, 376−379.
72. Magliozzo, R. S., McCracken, J., and Peisach, J. (1987) *Biochemistry 26*, 7923−7931.
73. Edmonds, D. T. (1977) *Phys. Lett. C 29*, 233−290.
74. Lucken, E. A. C. (1969) *Nuclear Quadrupole Coupling Constants*, Chapter 11, Academic Press, London.
75. McCracken, J., Pember, S., Benkovic, S. J., Villafranca, J. J., Miller, R. J. and Peisach, J. (1988) *J. Am. Chem. Soc. 110*, 1069−1074.
76. Pratt, J. M. (1983) *Inorg. Chim. Acta, 79*, 27.
77. Brown, K. L. (1986) *Inorg. Chem. 25*, 3111−3113.
78. Brown, K. L., and Evans, D. R. (1993) *Inorg. Chem. 32*, 2544−2548.
79. Eschenmosher, A. (1998) *Angew. Chem., Int. Ed. Engl. 27*, 5.

BI983067W